OPTICA QUANTUM

Nonlinear interferometry-based metrology of magneto-optical properties at infrared wavelengths

TANMOY CHAKRABORTY,[1] **THOMAS PRODUIT,**[1] **HARISH N. S. KRISHNAMOORTHY,**[2,3,4] **CESARE SOCI,**[2,3] **AND ANNA V. PATEROVA**[1,5,*]

[1] *A*⋆*STAR Quantum Innovation Centre (Q.InC), Institute of Materials Research and Engineering (IMRE), Agency for Science, Technology and Research (A*⋆*STAR), 2 Fusionopolis Way, Innovis #08-03, Singapore 138634, Singapore*
[2] *Centre for Disruptive Photonic Technologies, The Photonics Institute, Nanyang Technological University, 21 Nanyang Link, 637371, Singapore*
[3] *Division of Physics and Applied Physics, School of Physical and Mathematical Sciences, Nanyang Technological University, 21 Nanyang Link, Singapore 637371, Singapore*
[4] *Tata Institute of Fundamental Research Hyderabad, Gopanpally, Hyderabad 500046, Telangana, India*
[5] *Laboratory of Quantum Engineering of Light, South Ural State University, Chelyabinsk 454080, Russia*
*paterovaav@susu.ru

Received 19 July 2024; revised 29 December 2024; accepted 26 January 2025; published 12 February 2025

Magneto-optical properties of materials are utilized in numerous applications both in scientific research and industry. The novel properties of these materials can be further investigated by performing metrology in the infrared wavelength range, thereby enriching their potential applications. However, current infrared metrology techniques can be challenging and resource-intensive due to the unavailability of suitable components. To address these challenges, we propose and demonstrate a set of measurements based on nonlinear interferometry, which allows us to investigate magneto-optical properties of materials at infrared wavelength range by performing optical detection at the visible range. For a proof-of-principle study, we measure the Verdet constant of a bismuth iron garnet crystal, over a spectral bandwidth of 600 nm in the near-infrared range.

https://doi.org/10.1364/OPTICAQ.536867

1. INTRODUCTION

Infrared (IR) metrology is an active area of research, since a number of interesting physical properties of solid state and biological systems can be captured in the IR range [1,2], including Faraday rotation spectroscopy [3,4]. Conventional IR metrology techniques require light sources and detectors that operate at IR wavelengths. Hence, the efficiency of these techniques is limited by the performance of the existing IR detectors (above 3 μm wavelengths), which includes the need for their operation at cryogenic temperatures, which reduces their accessibility and ease of use [5–8]. Note that although the InGaAs-based detectors can perform optical detection efficiently at room temperature up to 3 μm [9], most of the detectors functional at 3–10 μm wavelength and beyond need cryogenic operations, see Ref. [5] for details. For instance, the efficiency of mercury cadmium telluride detectors is limited due to their high dark counts, low sensitivity even at cryogenic temperatures, and susceptibility to surrounding temperature fluctuations [5,10].

Alternatively, IR imaging and polarimetry can be performed by upconversion of the IR signal, where an additional high-power pump laser is employed to convert the wavelength of the IR photons to visible (or near-IR) wavelengths, where efficient detectors are easily available [11,12]. However, the necessity for a high-power laser may restrict the widespread application of this method.

Another method relies on the nonlinear interferometry of correlated photon pairs generated via spontaneous parametric downconversion (SPDC) [13–15], where one of the photons is generated at visible wavelength (signal), and the other at infrared (idler). In nonlinear interferometry, also known as SU(1,1) interferometry, the photon pairs are generated in two nonlinear crystals. An indistinguishability between SPDC photon pairs generated in these crystals is achieved by creating the path identity of the idler photons, which induces coherence between the signal photons. As a result, interference for signal photons becomes sensitive to the amplitude, phase, and polarization of the electric field of idler photons. Thus, light–matter interactions at IR wavelength can be studied by probing the sample with idler photons and analyzing the interference for the signal photons at visible wavelengths. The main advantage of this method is that it does not require a detector for IR, the detection can be performed at visible wavelengths, where efficient Si-based detectors are available. Additionally, SU(1,1) interferometry-based IR metrology provides superior signal-to-noise ratio compared with traditional direct IR detection methods [16]. With such nonlinear interferometry, a wide spectral tunability of the photons can be achieved by changing the phase matching within the same nonlinear crystal. The notion of “induced coherence without induced emission” was introduced by Wang *el. al.* [15], and later demonstrated in various applications, including spectroscopy

[13,17–26], imaging [26–35], holography [36], as well as optical coherence tomography [37–40]. Polarization degree-of-freedom of the photons in such schemes is exploited for metrology applications [41,42], tomography [43], and quantum erasers [44,45].

Through the present work, we demonstrate a polarimetry method for measuring the magneto-optical properties of materials at IR wavelengths. Our technique is based on nonlinear interferometry of non-degenerate SPDC photon pairs that are generated by optically pumping a nonlinear crystal, which is embedded into an SU(1,1) (Michelson type) interferometer. The idler photon generated at IR wavelength serves as the probing photon, while the signal photon generated at a visible/near-IR wavelength is detected. In such a system, any change in the polarization of the idler photons introduced by the magneto-optical properties of the sample at IR wavelength is inferred by studying the interference of the signal photons. For a proof-of-principle demonstration of our method, we measure the Vedet constant and saturation Faraday rotation of a $Bi_3Fe_5O_{12}$ (BIG) crystal in the wavelength range of 1540–2141 nm by performing detection at 820–708 nm, respectively.

2. THEORETICAL MODELS

The interference pattern of signal photons I_s in a nonlinear interferometer with optically active media at the idler arm of the interferometer is expressed as follows [42]:

$$I_s \propto 1 + |\tau_i|^2 |t||\mu| \cos(\phi_p - \phi_i - \phi_s + \Phi), \tag{1}$$

where $|\tau_i|$ is amplitude transmission coefficient for the idler photons through the optical components ($|\tau_i|^2$ accounts for the double pass of the infrared photons through the specimen); $|\mu|$ is the normalized correlation function for the SPDC photons; ϕ_p, ϕ_s, ϕ_i are acquired phases by pump, signal, and idler photons, respectively [14]; Φ is the initial phase in the interferometer. The parameter $|t|$ is polarization transfer which signifies the polarization component after passing through all the optical elements, which corresponds to the projection to the initial polarization state.

The visibility $\mathcal{V}$ of the interference pattern is defined from the maxima and minima of interference fringes and is proportional to the losses in the interferometer $|\tau_i|^2$, polarization transfer $|t|$, and correlation function $|\mu|$:

$$\mathcal{V} = \frac{I_s^{\max} - I_s^{\min}}{I_s^{\max} + I_s^{\min}} \propto |\tau_i|^2 |t||\mu|. \tag{2}$$

The parameter $|t|$ is calculated employing Jones matrix formalism [42]. Here we use combinations of half-wave plate (HWP), quarter-wave plates (QWP), and a polarizer to observe the Faraday rotation introduced by a sample and construct two schemes for the polarimetry measurements. For case I, the idler photons propagate through the HWP, the sample, the polarizer, then reflect from the mirror and travel back along the same path [see Fig. 1(a)]. For case II, the idler photons travel through the QWP and the sample, before reflecting back from the mirror [see Fig. 1(b)]. Thus, the parameter $|t|$ is defined by transformation matrices $\mathcal{M}_{\mathrm{HWP}}(\theta_{\mathrm{HWP}})$, $\mathcal{M}_{\mathrm{QWP}}(\theta_{\mathrm{QWP}})$, $\mathcal{M}_{\mathrm{P}}(\theta_{\mathrm{P}})$, $\mathcal{M}_{\mathrm{F}}(\theta_{\mathrm{F}})$, and $\mathcal{M}_{\mathrm{M}}$ for HWP, QWP, polarizer, the sample with Faraday rotation, and mirror, respectively (see appendix A). Here θ_{HWP}, θ_{QWP}, θ_{F}, and θ_{P} are the polarization rotation angles of the idler photons introduced by HWP, QWP, the sample, and the polarizer, respectively. Thus, in the scheme for case I the combined Jones matrix after a double pass through the optical components is given by

$$J_{\mathrm{I}} = \mathcal{M}_{\mathrm{HWP}}\, \mathcal{M}_{\mathrm{F}}\, \mathcal{M}_{\mathrm{P}}\, \mathcal{M}_{\mathrm{M}}\, \mathcal{M}_{\mathrm{P}}\, \mathcal{M}_{\mathrm{F}}\, \mathcal{M}_{\mathrm{HWP}}. \tag{3}$$

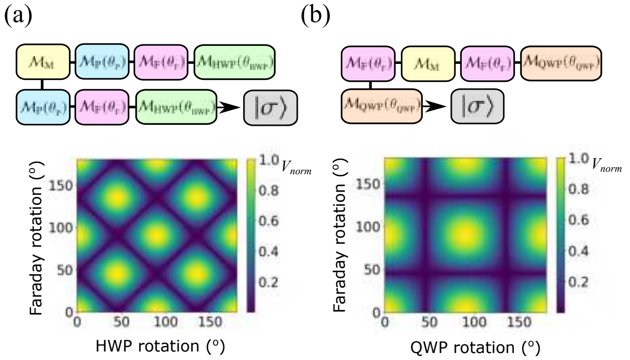

Fig. 1. Graphical representation of Jones matrix formalism and simulated two-dimensional mapping showing variation of normalized visibility as a function of Faraday rotation angle introduced by the sample and the rotation angle of the (a) HWP (with polarizer position fixed) and (b) QWP.

The initial state $|\sigma\rangle$ of vertically polarized idler photons can be written as $|\sigma\rangle = \begin{pmatrix} 0 & 1 \end{pmatrix}^{\mathsf{T}}$. Hence, the resulting polarization state of the idler photons is described as

$$|\sigma\rangle_{\mathrm{I}} = J_{\mathrm{I}} |\sigma\rangle. \tag{4}$$

Since interference visibility for the signal photons is proportional to $|t|$ from Eq. (1), the visibility for the interference of signal photons in this scheme is defined as a function of both θ_{HWP} and θ_{F} (see appendix A for more details),

$$\mathcal{V}^{\mathrm{I}} = |\cos(2\theta_{\mathrm{HWP}} + \theta_{\mathrm{F}}) \cos(2\theta_{\mathrm{HWP}} - \theta_{\mathrm{F}})|. \tag{5}$$

Next, the combined Jones matrix for case II can be written as

$$J_{\mathrm{II}} = \mathcal{M}_{\mathrm{QWP}}\, \mathcal{M}_{\mathrm{F}}\, \mathcal{M}_{\mathrm{M}}\, \mathcal{M}_{\mathrm{F}}\, \mathcal{M}_{\mathrm{QWP}}. \tag{6}$$

Then, in this case the normalized visibility as a function of θ_{QWP} and θ_{F} is given by

$$\mathcal{V}^{\mathrm{II}} = |\cos(\theta_{\mathrm{QWP}}) \cos(\theta_{\mathrm{F}})|. \tag{7}$$

Figure 1(a) [Fig. 1(b)] shows the mapping of normalized interference visibility as a function of the Faraday rotation angle by the sample and the angle of rotation of the HWP [QWP], calculated using Eq. (5) [Eq. (7)]. In both visibility maps, the higher values correspond to better indistinguishability of the idler photons, which is discussed more in detail in the following sections. In the experiments the visibilities can be measured depending on the orientation of the wave plates for a given applied magnetic field (or the introduced Faraday rotation). These measurements correspond to the horizontal cross sections of the graphs in Fig. 1.

3. EXPERIMENTAL SETUP AND MEASUREMENT PROTOCOLS

A simplified schematic of our experimental setup is shown in Fig. 2. Signal–idler SPDC photon pairs are generated by focusing the continuous-wave green laser (532 nm wavelength, 40 mW power, Laser Quantum) pump beam into a periodically

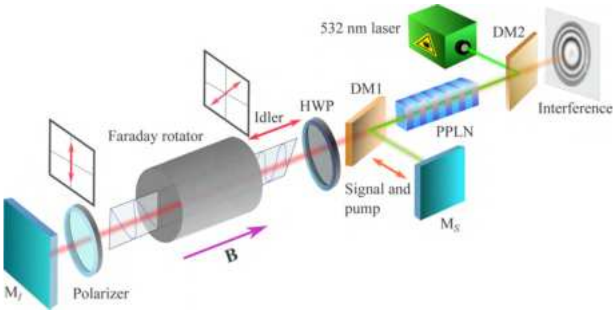

Fig. 2. Simplified schematic of the experimental setup based on an SU(1,1) interferometer: PPLN, periodically poled lithium niobate; DM1, dichroic mirror that transmits idler photons and reflects signal and pump photons; DM2, dichroic mirror that reflects pump and transmits signal; M_s and M_i, signal and idler mirrors, respectively. Interference of the signal photons are captured using the sCMOS camera.

poled lithium niobate (PPLN) nonlinear crystal (Covesion). The PPLN crystal consists of multiple periodic poling channels, each designed to meet different quasi-phase matching (QPM) conditions. QPM via different poling and temperature tuning allows generating idler photons over a 1500–2300 nm wavelength range, while conjugate signal photons are generated at 824 nm to 692 nm. After the PPLN crystal the co-propagating signal and idler beams are separated using a dichroic mirror (DM1) and collimated using two lenses, each with $f = 125$ mm focal length. The signal and idler photons propagate along the two arms of the SU(1,1) interferometer and reflect back from two metallic mirrors. The mirror M_i at the idler arm is mounted on a motorized translation stage, which allows us to introduce the additional phase for the idler photons. The pump beam following the signal path is reflected back by the mirror M_s into the PPLN crystal, which generates the signal and idler SPDC photons for the second time. After separating the signal and pump photons by a second dichroic mirror (DM2), the signal photons are focused onto a sCMOS camera (Thorlabs, Inc.). At the input of the sCMOS camera we use a notch at 532 nm and a bandpass filters to block any residual pump photons.

The BIG sample under study is placed in the path of idler photons (see the crystal structure of the sample and its magnetization properties given in appendix B). An externally applied magnetic field B to the sample along the optical axis results in Faraday rotation of the polarization of idler photons. Below the saturation field, the Faraday rotation angle Θ_F increases linearly with the strength of the applied magnetic field as follows:

$$\Theta_F = V(\lambda)Bl, \tag{8}$$

where l is length of the crystal along the light propagation direction (in our case $l = 0.38$ mm). Thus, at the linear regime of the Faraday rotation it is possible to measure the Verdet constant $V(\lambda)$.

To detect the Faraday rotation introduced by the sample we use two different configurations of the idler arm of the interferometer. In case I, after the DM1 idler photons pass through the HWP, BIG sample, and polarizer. The HWP introduces a known polarization transformation to idler photons, which is followed by Faraday rotation from the BIG crystal. Subsequently, the polarizer projects the polarization back to its initial vertically polarized state, as it was before the HWP. Note that this orientation of the polarizer remains unchanged for all the experiments presented here. After reflecting back from M_i, the idler photons travel back along the same path through the polarizer, BIG, and HWP. The polarization state of the vertically polarized photons is not changed by the polarizer, though it is altered by the Faraday rotation in the BIG crystal and the retardation introduced by the HWP. In case II, a known amount of retardation is introduced to the idler photons by QWP, which follows the Faraday rotation by the BIG crystal. These two operations are then applied in reverse order after the photons are reflected back by mirror M_i.

We analyze the resulting polarization state of the idler photons by measuring the visibilities of the interference fringes for the signal photons captured using the sCMOS camera. Note that the integration time for each of these measurements is 30 ms. These fringes are observed via introducing a relative phase by translating the mirror M_i along the optical axis of the idler arm. Thus, by capturing the variation of visibility pattern as a function of Faraday rotation angles at different applied magnetic fields B, we study the magneto-optical properties of BIG at IR wavelengths, according to Eqs. (5), (7), and (8).

4. EXPERIMENTAL RESULTS

First, we pump the PPLN crystal along a polling period that allows generation of the signal and idler photons at 813 nm and 1540 nm, respectively (see the signal spectrum in appendix C). The full-width at half-maximum of the spectrum is 1.4 ± 0.02 nm, which gives us $l_{\text{coh}} = 0.48 \pm 0.01$ mm coherence length. We measure the intensity of signal photons across ≈ 0.8 mm path length difference without and with the sample at the path of idler photons (see Figs. 8 and 9 in appendix C) and confirm the calculated coherence length experimentally. The inclusion of the BIG crystal into the path of idler arm changes the optical path length to ≈ 0.53 mm, which depends on the refractive index of BIG and its thickness l. In this case the optical path length difference can be compensated by shifting the position of the mirror M_i.

First, we perform interference measurements for cases I and II without introducing the BIG crystal into the interferometer (see Figs. 10 and 11 in appendix D for cases I and II, respectively). The visibility of the interference fringes depends on the orientation of the wave plates (θ_{HWP} for case I and θ_{QWP} for case II) as calculated by our theoretical model in Eq. (5) for case I and Eq. (7) for case II. Next, we introduce the BIG sample, balance the interferometer arms, and perform the polarimetry measurements.

4.1. Results for Case I: With HWP and Polarizer

We measure the visibility of the interference fringes for the signal photons with the orientation of the HWP at zero magnetic field $B = 0$ mT, which is shown in Fig. 3(a). The normalized visibility $\mathcal{V}$ is maximum when $\theta_{\text{HWP}} = 0°$. It reaches minimum value when $\theta_{\text{HWP}} = 45°$, and restores its maximum again when $\theta_{\text{HWP}} = 90°$, which is in accordance with Eq. (5) for $\theta_F = 0°$.

The visibility as a function of θ_{HWP} for different strengths of the magnetic field is shown in Fig. 3(a). Interestingly, initially one minimum in the visibility curve at $B = 0$ mT splits into two for $B \neq 0$ mT. The separation of these minima increases with the strength of the applied magnetic field and reaches a maximum for the saturation field. These results are consistent

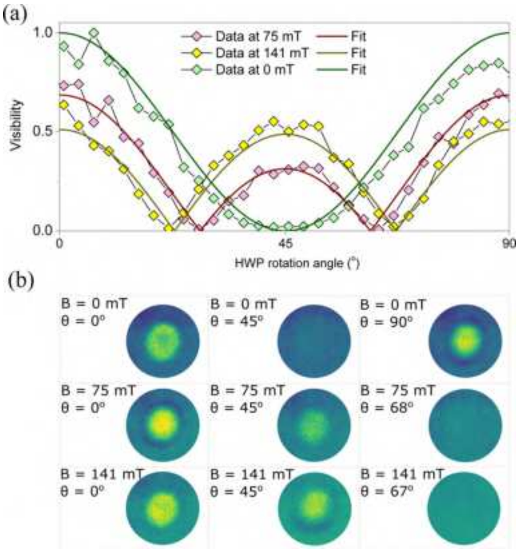

Fig. 3. (a) Visibility of interference fringes of signal photons depending on the rotation angle of the HWP at different magnetic field strengths applied to the BIG crystal. (b) Spatial intensity distribution of the signal photons revealing constructive interference patterns captured using the sCMOS camera. A few of such patterns are shown for different magnetic field strengths and HWP rotation angles.

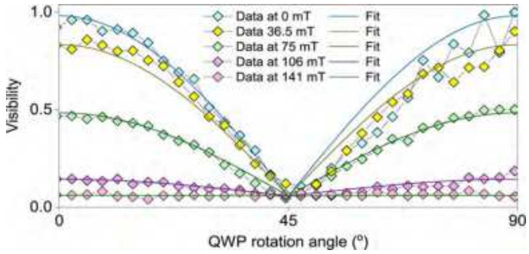

Fig. 4. Visibility of the interference fringes for the signal photons measured as a function of the rotation angle of QWP for different magnetic field strengths, causing different amounts of Faraday rotations.

with the theoretical model given by Eq. (5). We fit the experimental data for $B = 75$ mT and 141 mT, keeping θ_F as the fitting parameter, which yields $\theta_F = 34.08^\circ \pm 0.22^\circ$ and $44.34^\circ \pm 0.46^\circ$, respectively.

Change in the visibility of the interference pattern is associated with indistinguishability of SPDC photons generated in two passes of the pump beam through the nonlinear crystal. The Faraday rotator together with the wave plate and the polarizer change the polarization state of idler photons, which reduces the degree of indistinguishability and hence, the interference visibility of signal photons [42]. The stronger magnetic field causes larger Faraday rotation, reducing the degree of indistinguishability further. As an example, Fig. 3(b) shows a few measured spatial intensity distributions for constructive interference of signal photons for different values of θ_{HWP} and B.

4.2. Results for Case II: With QWP

In this scheme, we replace the HWP shown in Fig. 2 with a QWP, remove the polarizer, and perform manipulation of the input polarization of idler photons by rotating the QWP. The dependence of the visibility of the interference fringes on the orientation of the QWP for different values of B is shown in Fig. 4. For $B = 0$ mT and $\theta_{\mathrm{QWP}} = 0^\circ$, the photons generated during the forward and backward pass of the pump are indistinguishable, being in the same polarization state. However, the degree of indistinguishability is reduced with increasing θ_{QWP}, and the visibility of the interference fringes reaches a minimum when $\theta_{\mathrm{QWP}} = 45^\circ$. Additional polarization rotation introduced by the BIG varies with the strength of the magnetic field B, and the maximum visibility of the interference fringes are reduced by increasing the magnetic field strength. Visibility curves depending on the orientation of the QWP for each of the values of B are fitted to Eq. (7), whereas, the Faraday rotation angles caused by the BIG crystal are determined (see the summarized Faraday rotation angles depending on the applied magnetic field in Table 1 in appendix E). For the applied magnetic fields $B = 75$ mT and 141 mT the resulting Faraday rotation angles are $\theta_F = 31.24^\circ \pm 0.15^\circ$ and $44.9^\circ \pm 0.45^\circ$, respectively, which agree with the measured values in case I. It is worth noting that limited measurement resolution and possible occurrence of offsets while setting the orientations of the polarizer and the QWP have possibly resulted in the appearance of the minimum visibility in Fig. 4 at QWP rotation angles slightly higher than 45°. Fluctuations of the data points at higher QWP rotation angles can be attributed to the susceptibility of the interference visibility to mechanical vibrations caused by large rotations of the QWP by the motor and its larger backlash errors.

The motivation behind choosing two different polarimetry protocols is to validate our proposed IR metrology method with substantial experimental results obtained under different measurement settings. For instance, experiments in case I involve polarimetry with linear polarization states of the photons, whereas in case II, we investigate the evolution of elliptically polarized states. Additionally, note that the optical components used in our experiments introduce insertion losses, which can potentially alter the indistinguishability conditions of the photons and influence the visibility. However, by employing two different protocols, we investigate relative changes in visibility due to variations in the polarization states of the photons, while photon losses through the optical components remain constant across all polarization states. These observations establish that the indistinguishability of the photons is influenced by changes in polarization.

4.3. Wavelength Dependent Faraday Rotation

Next, we generate the idler photons at IR wavelengths ranging from $\lambda_{\mathrm{idler}} = 1516$ nm to 2141 nm. The coarse tuning of λ_{idler} is done by changing the poling period and fine-tuning is done by changing the applied temperature to the PPLN crystal while being in the same poling channel. Following the energy conservation law, the detected signal photons are generated in the range of 708 nm to 820 nm (see Table 2 in Appendix F for the details). To capture the dependence of the Verdet constant $V(\lambda)$ on wavelength we choose the scheme in case I of the interferometer, as both the maxima and the minima of the visibility undergo changes with the applied magnetic field. For each wavelength we capture Faraday rotations for different strengths of the applied magnetic field B. Following the same protocol as for the data captured at λ=1540 nm, we measure $V(\lambda)$ at IR wavelengths over 600 nm bandwidth range [see Fig. 5(a)].

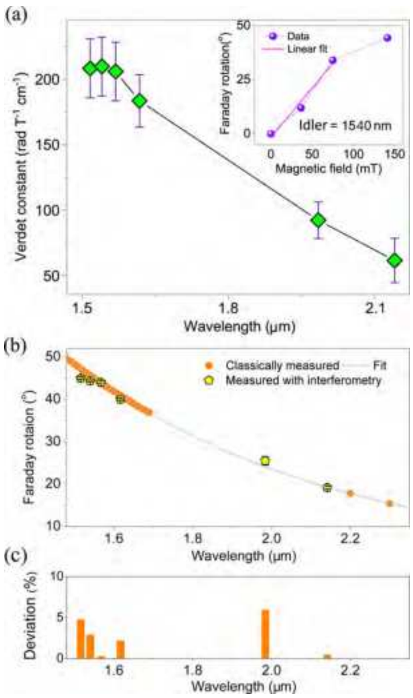

Fig. 5. (a) Verdet constant depending on wavelength. Points correspond to data measured employing the interferometry scheme. Inset shows Faraday rotations caused by the BIG crystal with applied magnetic field and its linear fit for $\lambda_{\text{idler}} = 1540$ nm. (b) Maximum Faraday rotation (at saturation magnetic field) introduced by the BIG sample depending on wavelength: the hexagons represent the experimental data measured in interferometry scheme, and the filled circles show the values provided by the manufacturer of the BIG crystal. The solid line represents the fit of a polynomial to these points. (c) Wavelength-dependent absolute values of deviation of our measured data from the fitted polynomial.

The estimated Faraday rotation angles for case I are plotted depending on B in the inset of Fig. 5(a). The data that are below the saturation field B_{sat} are fitted as a linear curve. The slope of the fit allows estimating the Verdet constant $V(\lambda)$ for a BIG crystal at $\lambda = 1540$ nm. Note that beyond the saturation field at $B = 150$ mT the Faraday rotation angle is $\theta_F = 45.0° \pm 0.5°$, which is consistent with the results of the magnetic characterization we perform for BIG and discussed in appendix B. The plot shows that $V(\lambda)$ decreases with the wavelength and becomes significantly small at 2141 nm. From the acquired data we also estimate the Faraday rotation angles at saturation magnetic field, which are shown in Fig. 5(b).

To quantitatively compare our results with the classically measured data obtained from Thorlabs, we proceed as follows. First, we fit the classical data to the polynomial described in Eq. (9) to a high degree of accuracy ($R^2 = 0.99999$):

$$f(\lambda) = 294.244 - 287.161\lambda + 100.910\lambda^2 - 12.502\lambda^3. \quad \textbf{(9)}$$

Next, we calculate the absolute deviations of our experimental data from the polynomial fit at different wavelengths and present the results in Fig. 5(c). It is evident that the deviations are small, with a maximum of approximately 6% at any given wavelength. This indicates that our measured values for wavelength-dependent saturation Faraday rotation are in good agreement with the classically measured data.

5. DISCUSSION AND CONCLUSIONS

To summarize, we have demonstrated a metrology scheme based on nonlinear interferometry to investigate the magneto-optical properties of a specimen at IR wavelengths. The method is implemented by using an SU(1,1) interferometer, where the paths of the signal and idler SPDC photons construct the two arms of the interferometer. Through our experiments, a polarization rotation of the idler photons introduced by the sample at IR wavelength is inferred by studying the interference of the signal photons. This allows us to perform the measurement of magneto-optical properties of the sample at IR wavelengths by performing detection at visible or near-IR wavelengths.

For a proof-of-concept demonstration of our method, we performed metrology of magneto-optical properties of $Bi_3Fe_5O_{12}$ crystal, which shows detectable Faraday rotation at IR wavelength range. We formulated theoretical analysis for calculating the visibility of the interference for signal photons as a function of the polarization rotation introduced by the sample at the idler photons wavelength. We captured the Verdet constant and Faraday rotation angles over a bandwidth from 1516 to 2141 nm, while the detection is performed at the range from 820 nm to 708 nm. The results obtained through our method show consistency with the classically measured data, which proves the applicability of our method. Note that our method is not particularly restricted to the above wavelength range, but rather can be functional over a broader wavelength region in the infrared domain. For instance, by choosing different QPM conditions in PPLN crystal used in the experiments, the metrology experiments can be performed at even longer wavelengths, up to 5 µm, which is given by the transparency range of the PPLN crystal. The method can be extended even further toward measuring materials which show detectable Faraday rotation at longer wavelengths (5–10 µm) using suitable nonlinear crystals like silver gallium sulfide [46] and gallium phosphide [47].

Although the article in Ref. [42] previously investigated the application of nonlinear interferometry for detecting polarization change, the present work advances significantly in terms of developing an infrared polarimetry method by bridging the domain of nonlinear interferometry with magneto-optics, exhibiting its validation with sufficient experimental results supported by theoretical models and applying it toward studying Faraday rotation of bismuth iron garnet in IR wavelengths. The proposed method and its experimental demonstration in the present paper open up possibilities for unleashing magneto-optical properties of a large class of materials, that is not yet well explored due to technical challenges [48,49]. Such investigations can reveal novel phenomena of these materials in the IR wavelength range, which can significantly boost their applications in scientific research and in industry. For instance, our method can be applied for performing polarimetry characterization of materials anticipating their applications as optical isolators at IR. Additionally, IR polarimetry can have applications in defense and facial recognition at night [50] and in characterization of painting materials [51]. These applications rely on polarimetry measurements of reflection and thermal emission from surfaces, which is rather complex to analyze. Such measurements can benefit from our IR polarimetry technique. Our method also provides a new path toward investigating light–matter interaction phenomena in novel material systems such as topological insulators, which have exotic surface states that are sensitive to the helicity of light [52,53].

APPENDIX A: CALCULATION OF THE INTERFERENCE VISIBILITIES FOR SCHEMES OF THE INTERFEROMETER IN CASE I AND CASE II

To calculate the parameter t expressed in Eq. (1), we first determine the transfer matrix for the optical components described in Section 3 for cases I and II. Change in the polarization of the idler photons by each of the optical components is determined by employing Jones matrix formalism. According to the schemes of the interferometer we express Jones matrices for HWP and QWP, Faraday rotator, polarizer, and a mirror as $\mathcal{M}(\theta_{\mathrm{HWP}})$, $\mathcal{M}(\theta_{\mathrm{QWP}})$, $\mathcal{M}(\theta_{\mathrm{F}})$, $\mathcal{M}_{\mathrm{P}}$, and $\mathcal{M}_{\mathrm{M}}$, respectively,

$$\mathcal{M}_{\mathrm{HWP}} = \begin{pmatrix} \cos 2\theta_{\mathrm{HWP}} & \sin 2\theta_{\mathrm{HWP}} \\ \sin 2\theta_{\mathrm{HWP}} & -\cos 2\theta_{\mathrm{HWP}} \end{pmatrix}, \tag{A1}$$

$$\mathcal{M}_{\mathrm{QWP}} = \frac{1}{\sqrt{2}} \begin{pmatrix} 1 + i\cos 2\theta_{\mathrm{QWP}} & i\sin 2\theta_{\mathrm{QWP}} \\ i\sin 2\theta_{\mathrm{QWP}} & 1 - i\cos 2\theta_{\mathrm{QWP}} \end{pmatrix}, \tag{A2}$$

$$\mathcal{M}_{\mathrm{F}} = \begin{pmatrix} \cos\theta_{\mathrm{F}} & \sin\theta_{\mathrm{F}} \\ -\sin\theta_{\mathrm{F}} & \cos\theta_{\mathrm{F}} \end{pmatrix}, \tag{A3}$$

$$\mathcal{M}_{\mathrm{P}} = \begin{pmatrix} 0 & 0 \\ 0 & 1 \end{pmatrix}, \mathcal{M}_{\mathrm{M}} = \begin{pmatrix} 1 & 0 \\ 0 & 1 \end{pmatrix}, \tag{A4}$$

where angles $\theta_{\mathrm{HWP,QWP,F}}$ denote angles between initial polarization state of the idler photons and an orientation of the wave plates, or Faraday rotation. In Eq. (A4) the matrix for polarizer $\mathcal{M}_{\mathrm{P}}$ is given for the vertical orientation, which is aligned with the initial polarization for the idler photons. The matrix $\mathcal{M}_{\mathrm{M}}$ is given by the unit matrix since the mirror does not alter the polarization of the propagating beams.

In case I, the polarization is changed by the HWP, BIG sample, and polarizer at the forward path along the arm of the SU(1,1) interferometer:

$$\mathcal{M}_1^{\mathrm{I}} = \mathcal{M}_{\mathrm{HWP}}\,\mathcal{M}_{\mathrm{F}}\,\mathcal{M}_{\mathrm{P}} = \begin{pmatrix} 0 & \sin(2\theta_{\mathrm{F}} + \theta_{\mathrm{HWP}}) \\ 0 & \cos(2\theta_{\mathrm{F}} + \theta_{\mathrm{HWP}}) \end{pmatrix}. \tag{A5}$$

After the reflection from M_i, the combined matrix is given in reverse order $\mathcal{M}_2^{\mathrm{I}} = \mathcal{M}_{\mathrm{P}}\,\mathcal{M}_{\mathrm{F}}\,\mathcal{M}_{\mathrm{HWP}}$. Hence the total transfer matrix is defined as

$$J_{\mathrm{I}} = \mathcal{M}_1^{\mathrm{I}}\,\mathcal{M}_{\mathrm{M}}\,\mathcal{M}_2^{\mathrm{I}} = \frac{1}{2} \begin{pmatrix} \cos 2\theta_{\mathrm{F}} - \cos 4\theta_{\mathrm{HWP}} & -\sin 2\theta_{\mathrm{F}} - \sin 4\theta_{\mathrm{HWP}} \\ \sin 2\theta_{\mathrm{F}} - \sin 4\theta_{\mathrm{HWP}} & \cos 2\theta_{\mathrm{F}} + \cos 4\theta_{\mathrm{HWP}} \end{pmatrix}. \tag{A6}$$

The initial state $|\sigma\rangle$ of vertically polarized idler photons can be written as $|\sigma\rangle = \begin{pmatrix} 0 & 1 \end{pmatrix}^{\mathsf{T}}$. The final state of the idler photons after using the Jones matrix and simplification of the equations is given by

$$|\sigma\rangle_{\mathrm{I}} = J_{\mathrm{I}} \begin{pmatrix} 0 \\ 1 \end{pmatrix} = \frac{1}{2} \begin{pmatrix} -\sin 2\theta_{\mathrm{F}} - \sin 4\theta_{\mathrm{HWP}} \\ \cos 2\theta_{\mathrm{F}} + \cos 4\theta_{\mathrm{HWP}} \end{pmatrix}. \tag{A7}$$

The resulting interference depends on the vertical polarization component. Thus, the visibility of the interference fringes depends on the orientation of the HWP and the Faraday rotation as follows:

$$\mathcal{V}^{\mathrm{I}} = \frac{1}{2}|(\cos 2\theta_{\mathrm{F}} + \cos 4\theta_{\mathrm{HWP}})| = |\cos(2\theta_{\mathrm{HWP}} + \theta_{\mathrm{F}})\cos(2\theta_{\mathrm{HWP}} - \theta_{\mathrm{F}})|. \tag{A8}$$

Similarly, in case II, the matrix for combined QWP and BIG crystal is given by

$$\mathcal{M}_1^{\mathrm{II}} = \frac{\sqrt{2}}{2} \begin{pmatrix} \cos\theta_{\mathrm{F}} + i\cos(2\theta_{\mathrm{QWP}} + \theta_{\mathrm{F}}) & \sin\theta_{\mathrm{F}} + i\sin(2\theta_{\mathrm{QWP}} + \theta_{\mathrm{F}}) \\ -\sin\theta_{\mathrm{F}} + i\sin(2\theta_{\mathrm{QWP}} + \theta_{\mathrm{F}}) & \cos\theta_{\mathrm{F}} - i\cos(2\theta_{\mathrm{QWP}} + \theta_{\mathrm{F}}) \end{pmatrix}. \tag{A9}$$

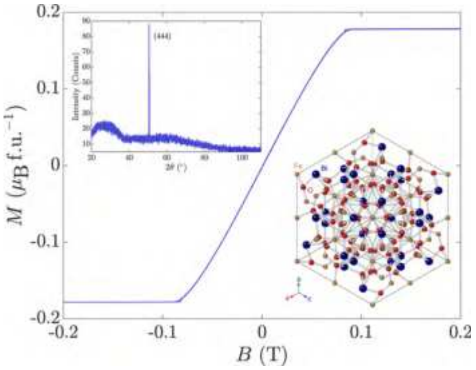

Fig. 6. Isothermal magnetization data as a function of applied magnetic field. The upper inset shows single-crystal θ-2θ x ray diffraction scan data and the lower inset shows the cubic lattice structure of BIG.

Hence, the Jones matrix for double-pass configuration is $J_{\mathrm{II}} = \mathcal{M}_1^{\mathrm{II}}\,\mathcal{M}_{\mathrm{M}}\,\mathcal{M}_2^{\mathrm{II}}$. The final visibility depending on the orientation of the QWP and the Faraday rotation by the BIG sample is given by

$$\mathcal{V}^{\mathrm{II}} = |\cos(\theta_{\mathrm{QWP}})\cos(\theta_{\mathrm{F}})|. \tag{A10}$$

APPENDIX B: CHARACTERIZATION OF THE $\mathrm{BI_3FE_5O_{12}}$ SAMPLE

We perform magnetization and x ray diffraction (XRD) measurements for characterizing of $\mathrm{B_3Fe_5O_{12}}$ crystal used in our measurements. Figure 6 shows the isothermal magnetization curve measured (using a superconducting quantum interference-based magnetometer by Quantum Design) as a function of externally applied magnetic field at 300 K. The data shows that magnetization saturates when the magnetic field is approximately 100 mT, which is consistent with the magnetic-field-dependent Faraday rotation results shown in the inset of Fig. 5(a). The upper inset of Fig. 6 shows the θ–2θ XRD scanning depicting only the (444) peak, that confirms the single crystallinity of the BIG sample [54,55]. The unit cell is cubic with $a = 12.493$ Å (see the lower inset of Fig. 6).

APPENDIX C: COHERENCE LENGTH OF THE IDLER PHOTONS AT 1540 NM

The spectrum of the signal SPDC photons generated from PPLN crystal with 7.4 µm poling periodicity and T=126°C applied temperature is shown in Fig. 7. The central wavelength of the spectrum is 813 ± 0.2 nm, the bandwidth is 1.40 ± 0.02 nm, which gives the 0.48 ± 0.01 mm coherence length.

An initial assessment of the coherence length of the photons is necessary to estimate the translation limit of the idler mirror M_i within which, we can observe interference. Once having this knowledge, constraining our measurements within this limit ensures capturing the interference fringes of the signal photons. Importantly, capturing the fringes across the total coherence length allows us to identify the position of M_i where the visibility of the fringes is a maximum. We perform all our measurements across this position of M_i to obtain the maximum possible signal-to-noise ratio.

Intensity of the signal photons captured as a function of the translation of M_i (MTS25/M, Thorlabs Inc.) shows the

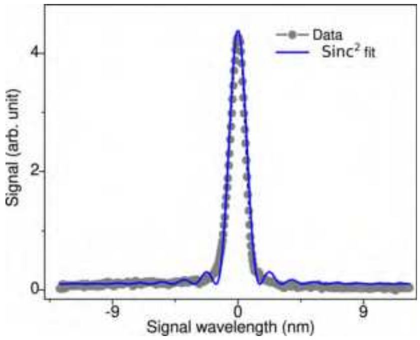

Fig. 7. Optical spectrum of the signal photons at 813 nm. The data is fitted to a sinc^2 curve. The linewidth is 1.40 ± 0.02 nm, which is the QPM bandwidth of the photons at near-IR range.

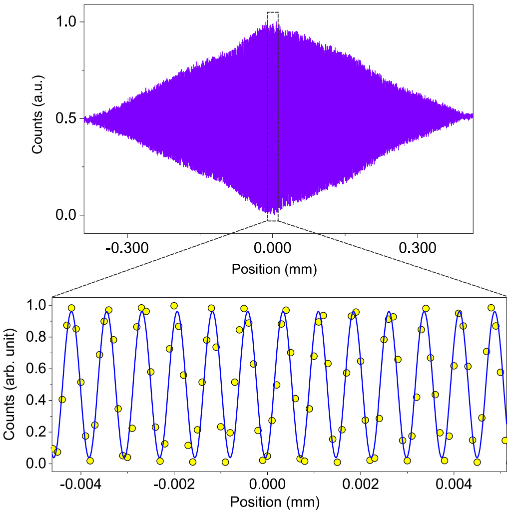

Fig. 8. Interference fringes depending on the additional phase introduced by translating mirror M_i of the interferometer when the sample is absent. The inset shows an enlarged view of the interference data around the balanced position of the interferometer and its fit to a cosine function.

interference of the signal photons in Fig. 8. The interference is observable within the coherence length of ≈ 0.44 of the SPDC photons, which is twice the width of the envelope (due to double pass configuration) taken at the $1/e$ amplitude decay of the interference fringes [56], see Fig. 8. In the balanced position of the interferometer, the visibility of the interference is a maximum. The inset at the bottom of Fig. 8 shows an enlarged view of the interference fringes close to the balanced position of the interferometer. Due to the double-pass along the arms of the SU(1,1) interferometer, the periodicity of the interference fringes corresponds to half of the idler wavelength. Fitting the data to a cosine curve gives the periodicity of the interference fringes, which is 759 nm. We attribute the error in this value to the irreversibility caused by the backlash error of the translation stage and other mechanical components.

The interference fringes after the insertion of the BIG crystal into the idler arm of the interferometer are shown in Fig. 9. Due to change in the optical path length, the balanced position of the interferometer is shifted by 0.53 mm. This change of the optical path length corresponds to the 0.38 mm thickness of the BIG sample and depends on the wavelength of the idler photons (as refractive index of a medium varies with wavelength of the light according to the Sellmeier relation [57]). The inset at the bottom in Fig. 9 shows an enlarged view of the interference fringes and their fit to cosine curve.

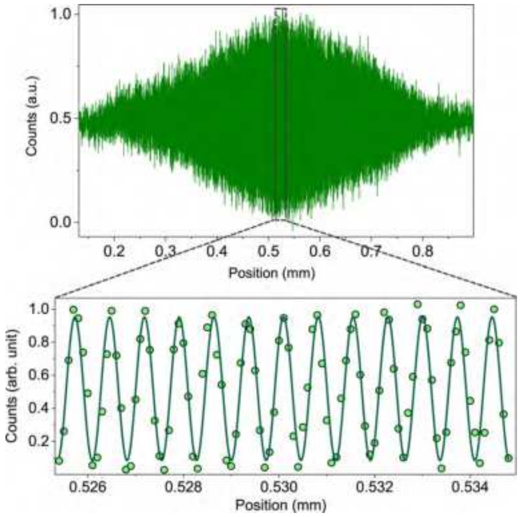

Fig. 9. Interference fringes depending on the translation of the mirror M_i when the sample is present. The interference fringes at the optical path length difference of 0.53 mm are shown in the inset. The fitting is performed using a cosine function.

APPENDIX D: VISIBILITY OF THE INTERFERENCE WITHOUT THE SAMPLE

In case I, in the absence of a BIG sample, the visibility of interference fringes for signal photons depends on the orientation of the HWP and polarizer (see the inset in Fig. 10). Since the polarizer is aligned with the initial polarization of the idler photons, the visibility of the interference is given by the orientation of the HWP only. For each rotation angle of the HWP we introduce additional phase into the interferometer by translating mirror M_i over a few periods of λ_{idler}, capture the interference fringes, and estimate the visibilities, see Fig. 10(a). The constructive interference pattern of the signal photons captured by the sCMOS camera at angles of HWP at 0°, 45°, and 90° are shown in Fig. 10(b).

In case II, when we replace the HWP by a QWP and remove the polarizer (see the inset of Fig. 11(a)), the balance condition for the interferometer changes. We balance the interferometer by translating the mirror M_i. Next, we record the change in visibility of the interference depending on the orientation of QWP in the absence of the BIG sample (see Fig. 11(a)). Likewise, the constructive interference pattern of the signal photons at orientation angles of QWP at 0°, 45°, and 90° are shown Fig. 11(b). Both of the obtained visibility data are in a good agreement with the theoretical analysis given by Eq. (5) (case I) and Eq. (7) (case II).

To determine the interference visibility, for each position of the idler mirror M_i, we integrate the intensity counts of the signal photons over a specific number of pixels from the central fringe of the interference pattern captured by the camera. (Notably, the spatial extent of these pixels is significantly smaller than that of the central fringe itself.) The integrated

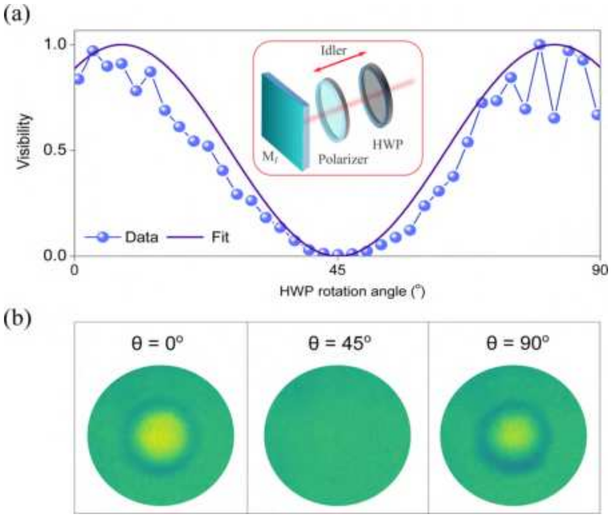

Fig. 10. (a) Visibility of the interference at the absence of the sample as a function of HWP orientation. (b) Examples of the constructive interference pattern captured by sCMOS camera at a few orientation angles of the HWP.

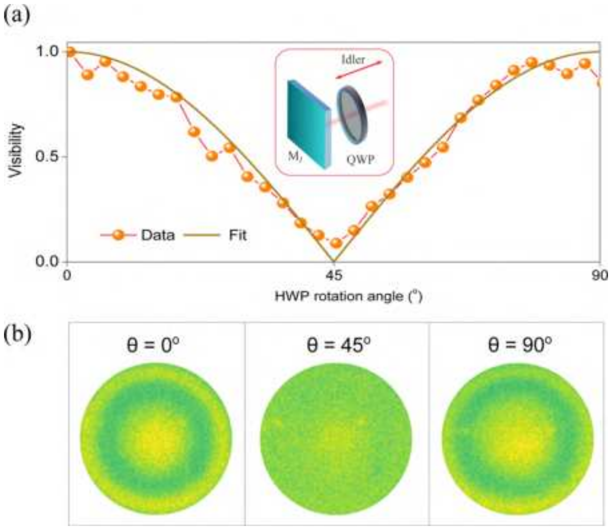

Fig. 11. (a) Visibility of the interference at the absence of the sample as a function of QWP orientation. (b) Examples of the constructive interference pattern captured by sCMOS camera at a few orientation angles of the QWP.

counts I_s vary sinusoidally with the position of the mirror M_i, exhibiting maximum (I_s^{max}) and minimum (I_s^{min}) values, which correspond to constructive and destructive interferences, respectively. These extrema are obtained by fitting the data to a sinusoidal function. The visibility is then calculated using the formula $(I_s^{max} - I_s^{min})/(I_s^{max} + I_s^{min})$.

APPENDIX E: FARADAY ROTATION ANGLES MEASURED VIA NONLINEAR INTERFEROMETRY

In Table 1 we show the experimentally measured Faraday rotations depending on the applied magnetic fields in case I and II.

Table 1. Applied magnetic field strengths and measured Faraday rotations

Magnetic field (case I)	Faraday rotation(case I)
75 ± 8 mT	34.08° ± 0.22°
141 ± 15 mT	44.34° ± 0.46°
Magnetic field (case II)	**Faraday rotation(case II)**
36.5 ± 3.9 mT	16.46° ± 0.47°
75 ± 8 mT	31.24° ± 0.15°
106 ± 4.1 mT	42.31° ± 0.08°
141 ± 15 mT	44.9° ± 0.45°

APPENDIX F: WAVELENGTH-DEPENDENT FARADAY ROTATION

To perform metrology of the Verdet constant and the Faraday rotation at the saturation magnetic field over a broad IR wavelength range, we generate the idler photons in the range of 1540 nm to 2141 nm by pumping the PPLN through different quasi-phase-matched channels and setting the corresponding temperatures. We measure the signal (visible/near-IR) photon spectra using a spectrometer (HR4000, Ocean Optics) and determine the signal wavelengths. Following the energy conservation, we determine the wavelengths of idler photons. Table 2 summarizes signal (λ_{signal}) and idler (λ_{idler}) wavelengths,

Table 2. Poling periods of the PPLN and temperatures for generating signal and idler photons at different wavelengths. The wavelength of the pump laser is 532 nm in all these cases

Polling period	Temperature	Signal wavelength (detected)	Idler wavelength (Probed)
7.4 µm	378 K	820 nm	1516 nm
7.4 µm	399 K	813 nm	1540 nm
7.4 µm	423 K	805 nm	1568 nm
7.71 µm	303 K	793 nm	1617 nm
8.36 µm	352 K	725 nm	2000 nm
8.36 µm	571 K	708 nm	2141 nm

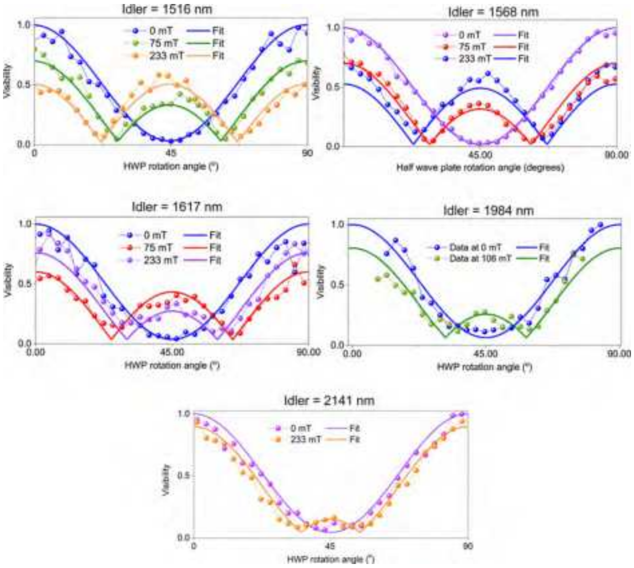

Fig. 12. Variation of visibilities of interference of the signal photons with the rotation angle of the HWP for different idler wavelengths.

with corresponding values of the polling periods and PPLN temperatures.

For each of these cases, we measure visibility of the interfering signal photons as a function of the input polarization of the idler photons. Figure 12 shows the visibilities of the interference pattern depending on HWP rotation angle (protocol for the case I) and their fit using Eq. (5). We determine θ_F from the fitting and estimate the Verdet constant. For the estimation of the Verdet constant we choose the magnetic fields below the saturation field. At the saturation magnetic field we calculate the Faraday rotation angles as a function of wavelength.

Funding. National Research Foundation Singapore (NRF2021-QEP2-03-P08); Agency for Science, Technology and Research (C230917004); Ministry of Science and Higher Education of the Russian Federation (075-15-2024-634).

Acknowledgements. We thank Jian Rui Soh and Vytautas Valuckas for their help with characterizing the sample.

Disclosures. The authors declare no conflicts of interest.

Data availability. Data presented in the paper are not publicly available but can be obtained from the authors upon reasonable request.

REFERENCES

1. P. Colarusso, L. H. Kidder, I. W. Levin, *et al.*, "Infrared spectroscopic imaging: from planetary to cellular systems," Appl. Spectrosc. **52**, 106A–120A (1998).
2. R. Bhargava, "Infrared spectroscopic imaging: the next generation," Appl. Spectrosc. **66**, 1091–1120 (2012).
3. R. Lewicki, J. H. Doty III, R. F. Curl, *et al.*, "Ultrasensitive detection of nitric oxide at 5.33 µm by using external cavity quantum cascade laser-based Faraday rotation spectroscopy," Proc. Natl. Acad. Sci. U.S.A. **106**, 12587–12592 (2009).
4. C. Liu, Y. Hai, and A. Dang, "Faraday rotation and ellipticity spectroscopy between excited states of Rb vapor: theory and experiment," Phys. Rev. A **107**, 053105 (2023).
5. S. Bianconi and H. Mohseni, "Recent advances in infrared imagers: toward thermodynamic and quantum limits of photon sensitivity," Rep. Prog. Phys. **83**, 044101 (2020).
6. J. Chen, J. Wang, X. Li, *et al.*, "Recent progress in improving the performance of infrared photodetectors via optical field manipulations," Sensors **22**, 677 (2022).
7. A. Rogalski, "Infrared detectors: status and trends," Prog. Quantum Electron. **27**, 59–210 (2003).
8. Y. Wang, J. Li, H. Sun, *et al.*, "A review on the developments and space applications of mid- and long-wavelength infrared detection technologies," Front. Inf. Technol. Electron. Eng. **25**, 1031–1056 (2024).
9. Y. Miao, H. Lin, B. Li, *et al.*, "Review of Ge(GeSn) and InGaAs avalanche diodes operating in the SWIR spectral region," Nanomaterials **13**, 606 (2023).
10. W. Lei, J. Antoszewski, and L. Faraone, "Progress, challenges, and opportunities for HgCdTe infrared materials and detectors," Appl. Phys. Rev. **2**, 041303 (2015).
11. S. Junaid, S. C. Kumar, M. Mathez, *et al.*, "Video-rate, mid-infrared hyperspectral upconversion imaging," Optica **6**, 702–708 (2019).
12. Z. Zhu, D. Zhang, F. Xie, *et al.*, "Nonlinear polarization imaging by parametric upconversion," Optica **9**, 1297–1302 (2022).
13. D. A. Kalashnikov, A. V. Paterova, S. P. Kulik, *et al.*, "Infrared spectroscopy with visible light," Nat. Photonics **10**, 98–101 (2016).
14. A. Paterova, H. Yang, C. An, *et al.*, "Measurement of infrared optical constants with visible photons," New J. Phys. **20**, 043015 (2018).
15. L. Wang, X. Zou, and L. Mandel, "Induced coherence without induced emission," Phys. Rev. A **44**, 4614–4622 (1991).
16. Y. Mukai, R. Okamoto, and S. Takeuchi, "Quantum Fourier-transform infrared spectroscopy in the fingerprint region," Opt. Express **30**, 22624–22636 (2022).
17. A. V. Paterova and L. A. Krivitsky, "Nonlinear interference in crystal superlattices," Light: Sci. Appl. **9**, 82 (2020).
18. K. A. Kuznetsov, E. I. Malkova, R. V. Zakharov, *et al.*, "Nonlinear interference in the strongly nondegenerate regime and Schmidt mode analysis," Phys. Rev. A **101**, 053843 (2020).
19. A. Paterova, S. Lung, D. Kalashnikov, *et al.*, "Nonlinear infrared spectroscopy free from spectral selection," Sci. Rep. **7**, 42608 (2017).
20. M. Kutas, B. Haase, J. Klier, *et al.*, "Quantum-inspired terahertz spectroscopy with visible photons," Optica **8**, 438–441 (2021).
21. A. Burlakov, S. Kulik, A. Penin, *et al.*, "Three-photon interference: spectroscopy of linear and nonlinear media," J. Exp. Theor. Phys. **86**, 1090–1097 (1998).
22. S. Kulik, G. Maslennikov, S. Merkulova, *et al.*, "Two-photon interference in the presence of absorption," J. Exp. Theor. Phys. **98**, 31–38 (2004).
23. D. Klyshko, "Ramsey interference in two-photon parametric scattering," JETP **104**, 2676–2684 (1993).
24. K. Hashimoto, D. B. Horoshko, M. I. Kolobov, *et al.*, "Fourier-transform infrared spectroscopy with undetected photons from high-gain spontaneous parametric down-conversion," Commun. Phys. **7**, 217 (2024).
25. P. Kaufmann, H. M. Chrzanowski, A. Vanselow, *et al.*, "Mid-IR spectroscopy with NIR grating spectrometers," Opt. Express **30**, 5926–5936 (2022).
26. C. Lindner, J. Kunz, S. J. Herr, *et al.*, "Nonlinear interferometer for Fourier-transform mid-infrared gas spectroscopy using near-infrared detection," Opt. Express **29**, 4035–4047 (2021).
27. G. B. Lemos, V. Borish, G. D. Cole, *et al.*, "Quantum imaging with undetected photons," Nature **512**, 409–412 (2014).
28. E. Pearce, N. R. Gemmell, J. Flórez, *et al.*, "Practical quantum imaging with undetected photons," Opt. Continuum **2**, 2386–2397 (2023).
29. A. V. Paterova, H. Yang, Z. S. Toa, *et al.*, "Quantum imaging for the semiconductor industry," Appl. Phys. Lett. **117**, 054004 (2020).
30. A. V. Paterova, S. M. Maniam, H. Yang, *et al.*, "Hyperspectral infrared microscopy with visible light," Sci. Adv. **6**, eabd0460 (2020).
31. Y. Yang, H. Liang, X. Xu, *et al.*, "Interaction-free, single-pixel quantum imaging with undetected photons," npj Quantum Inf **9**, 2 (2023).
32. E. A. Santos, T. Pertsch, F. Setzpfandt, *et al.*, "Subdiffraction quantum imaging with undetected photons," Phys. Rev. Lett. **128**, 173601 (2022).
33. J. Fuenzalida, M. Gilaberte Basset, S. Töpfer, *et al.*, "Experimental quantum imaging distillation with undetected light," Sci. Adv. **9**, eadg9573 (2023).
34. M. Gilaberte Basset, F. Setzpfandt, F. Steinlechner, *et al.*, "Perspectives for applications of quantum imaging," Laser Photonics Rev. **13**, 1900097 (2019).
35. I. Kviatkovsky, H. M. Chrzanowski, E. G. Avery, *et al.*, "Microscopy with undetected photons in the mid-infrared," Sci. Adv. **6**, eabd0264 (2020).
36. S. Töpfer, M. Gilaberte Basset, J. Fuenzalida, *et al.*, "Quantum holography with undetected light," Sci. Adv. **8**, eabl4301 (2022).
37. A. V. Paterova, H. Yang, C. An, *et al.*, "Tunable optical coherence tomography in the infrared range using visible photons," Quantum Sci. Technol. **3**, 025008 (2018).
38. A. Vallés, G. Jiménez, L. J. Salazar-Serrano, *et al.*, "Optical sectioning in induced coherence tomography with frequency-entangled photons," Phys. Rev. A **97**, 023824 (2018).
39. A. Vanselow, P. Kaufmann, I. Zorin, *et al.*, "Frequency-domain optical coherence tomography with undetected mid-infrared photons," Optica **7**, 1729–1736 (2020).
40. G. J. Machado, G. Frascella, J. P. Torres, *et al.*, "Optical coherence tomography with a nonlinear interferometer in the high parametric gain regime," Appl. Phys. Lett. **117**, 1 (2020).
41. T. Grayson, J. Torgerson, and G. Barbosa, "Observation of a nonlocal Pancharatnam phase shift in the process of induced coherence without induced emission," Phys. Rev. A **49**, 626–628 (1994).

42. A. Paterova, H. Yang, C. An, *et al.*, "Polarization effects in nonlinear interference of down-converted photons," Opt. Express **27**, 2589–2603 (2019).
43. J. Fuenzalida, J. Kysela, K. Dovzhik, *et al.*, "Quantum state tomography of undetected photons," Phys. Rev. A **109**, 022413 (2024).
44. T. J. Herzog, P. G. Kwiat, H. Weinfurter, *et al.*, "Complementarity and the quantum eraser," Phys. Rev. Lett. **75**, 3034–3037 (1995).
45. N. R. Gemmell, Y. Ma, E. Pearce, *et al.*, "Coupling undetected sensing modes by quantum erasure," arXiv (2023).
46. M. Kumar, P. Kumar, A. Vega, *et al.*, "Mid-infrared photon pair generation in $AgGaS_2$," Appl. Phys. Lett. **119**, 244001 (2021).
47. D. J. Wilson, K. Schneider, S. Hönl, *et al.*, "Integrated gallium phosphide nonlinear photonics," Nat. Photonics **14**, 57–62 (2020).
48. D. Vojna, O. Slezák, A. Lucianetti, *et al.*, "Verdet constant of magneto-active materials developed for high-power Faraday devices," Appl. Sci. **9**, 3160 (2019).
49. D. Vojna, O. Slezák, R. Yasuhara, *et al.*, "Faraday rotation of Dy_2O_3, CeF_3 and $Y_3Fe_5O_{12}$ at the mid-infrared wavelengths," Materials **13**, 5324 (2020).
50. G. Bieszczad, S. Gogler, and J. Świderski, "Review of design and signal processing of polarimetric imaging cameras," Opto-Electron. Rev. **29**, 1 (2021).
51. N. Hagen, "Review of thermal infrared polarimetry, I: theory," Opt. Eng. **61**, 070902 (2022).
52. H. N. Krishnamoorthy, A. M. Dubrovkin, G. Adamo, *et al.*, "Topological insulator metamaterials," Chem. Rev. **123**, 4416–4442 (2023).
53. G. Spektor, A. David, G. Bartal, *et al.*, "Spin-patterned plasmonics: towards optical access to topological-insulator surface states," Opt. Express **23**, 32759–32765 (2015).
54. S. Flament, L. Warsito, L. Mechin, *et al.*, "Magneto-optic laser deposited $Bi_3Fe_5O_{12}/Gd_3Ga_5O_{12}$ (111) films: characterization and imaging," Trans. Magn. Soc. Jpn **2**, 214–215 (2002).
55. N. Adachi, T. Okuda, V. Denysenkov, *et al.*, "Magnetic properties of single crystal film $Bi_3Fe_5O_{12}$ prepared onto $Sm_3(Sc, Ga)_5O_{12}(111)$," J. Magn. Magn. Mater. **242-245**, 775–777 (2002).
56. D. Lopez-Mago and L. Novotny, "Coherence measurements with the two-photon Michelson interferometer," Phys. Rev. A **86**, 023820 (2012).
57. A. Djalalian-Assl, "Tailoring properties of magneto-optical photonic crystals," arXiv (2019).